



Deposited via The University of Leeds.

White Rose Research Online URL for this paper:

<https://eprints.whiterose.ac.uk/id/eprint/104361/>

Version: Accepted Version

---

**Article:**

Tranter, TG, Gostick, JT, Gale, WF et al. (2016) Pore Network Modeling of Compressed Fuel Cell Components with OpenPNM. *Fuel Cells*, 16 (4). pp. 504-515. ISSN: 1615-6846

<https://doi.org/10.1002/fuce.201500168>

---

© 2016 WILEY-VCH Verlag GmbH & Co. KGaA, Weinheim. This is the peer reviewed version of the following article: "Tranter, T. G., Gostick, J. T., Burns, A. D. and Gale, W. F. (2016), Pore Network Modeling of Compressed Fuel Cell Components with OpenPNM. *Fuel Cells*, 16: 504–515" which has been published in final form at <http://dx.doi.org/10.1002/fuce.201500168>. This article may be used for non-commercial purposes in accordance with Wiley Terms and Conditions for Self-Archiving.

**Reuse**

Items deposited in White Rose Research Online are protected by copyright, with all rights reserved unless indicated otherwise. They may be downloaded and/or printed for private study, or other acts as permitted by national copyright laws. The publisher or other rights holders may allow further reproduction and re-use of the full text version. This is indicated by the licence information on the White Rose Research Online record for the item.

**Takedown**

If you consider content in White Rose Research Online to be in breach of UK law, please notify us by emailing [eprints@whiterose.ac.uk](mailto:eprints@whiterose.ac.uk) including the URL of the record and the reason for the withdrawal request.

# Pore network modelling of compressed fuel cell components with OpenPNM

**T.G. Tranter (1), A.D. Burns (1), J.T. Gostick (2), W.F. Gale(1)\***

(1) Centre for Integrated Energy Research, School of Chemical and Process Engineering,  
University of Leeds, LS2 9JT, UK

(2) Department of Chemical Engineering, McGill University, Montreal, QC H3A 0GA,  
Canada

Tel.: +44-113-343-2498

Fax: +44-113-343-7310

w.f.gale@leeds.ac.uk

## Abstract

Pore network modelling is used to model water invasion and multiphase transport through compressed PEFC gas diffusion layers. Networks are created using a Delaunay tessellation of randomly placed base-points setting the pore locations and its complement, the Voronoi diagram, is used to define the location of fibers and resultant pore and throat geometry.

The model is validated in comparison to experimental capillary pressure curves obtained on compressed and uncompressed materials. Primary drainage is simulated with an invasion percolation algorithm that sequentially invades pores and throats separately with excellent agreement to experimental data, but required a slight modification to account for the higher aspect ratio of compressed pores.

Compression is simulated by scaling the through-plane coordinates in a uniform manner simulating a GDL wholly beneath the current-collector land. The relative permeability and diffusivity show some dependence on uniform compression. In-plane porosity variations introduced by land-channel compression are also investigated which have a marked effect on the limiting current. Saturation at breakthrough does not appear to be dependent on compression but a more important parameter, namely the peak saturation, is shown to influence the fuel cell performance and is dependent on the percolation inlet conditions.

## 1. Introduction

Understanding the multiphase processes occurring within polymer electrolyte fuel cells (PEFC) has been the focus of many studies over the years, yet gaps in the knowledge still remain owing largely to the unusual or atypical properties of the porous electrode components. The gas diffusion layer (GDL), catalyst layer (CL), microporous layer (MPL) and membrane are all porous and vary in porosity, thickness, permeability, wettability and anisotropy. One particular knowledge gap is how the multiphase transport processes throughout the porous media are affected by the morphological changes occurring upon compression when assembling the fuel cell.

A summary of the experimental and numerical studies of the various effects of compression on the GDL can be found in our previous work [1]. In general the effective transport properties (permeability and diffusivity) of the GDL are decreased with compression due to the reduced pore volume and connectivity, while electrical and thermal conductivity increase as contact resistance is reduced. PEFCs operating at high current density experience increased saturation of liquid water owing to increased water production at the catalyst layer and condensation from humidified gasses. Therefore, the relative transport properties of each phase (gas and liquid) are also important to consider and as yet few experimental studies have been performed to understand how compression may affect multiphase flow. Gostick et al [2] measured air-water capillary pressure curves on compressed samples and found that compressing increased the required entry pressure for water, indicating that throat sizes were decreased. Results from Bazylak et al. [3] and Mortazavi and Tajiri [4] suggest that compression actually alters the pathways taken by liquid water, presumably because compression alters some pores/throats more than others as well as changes to wettability. Ramos-Alvarado et al. have shown that the relative permeability of the liquid phase may also increase with compression [5], although they acknowledge that their measurement was very difficult to obtain. Markötter et al. have used synchrotron x-ray imaging to show that liquid water transport is heavily influenced by the local structure with fiber orientation playing a key role [6]. Modelling is therefore important to understand the underlying reasons for these changes in multiphase transport and could lead to insights and future design improvements for fuel cell components. A key feature of the present model is the realistic representation of the fibrous structure and its morphological changes under compression, allowing the impact of compression to arise naturally.

Computational fluid dynamics (CFD) has been used to investigate the effects of compression on multiphase flow through an idealized GDL [1]. Compression was found to induce through-plane liquid fingering as the in-plane (IP) pathways begin to close off, increasing transport resistance. However, the model could only produce limited information due to expense and limited domain size. Therefore, relative transport relations could not be deduced. Pore Network Models (PNMs) are useful tools for analyzing the transport characteristics of porous fuel cell components, especially for multiphase conditions. Simple and efficient percolation algorithms can be performed, since transport is capillary dominated [7]. The general concept of PNMs is to map the pore space onto a discrete network of pores and connecting throats, then to conduct simulations using transport algorithms based upon nodal balances (i.e. resistor networks) of the transported fluids. In addition to speed and simplicity, PNMs have some advantages over the more widely used continuum models [8]. PNMs can resolve realistic saturation profiles [9], and have a direct connection between the structure and topology of the porous material and transport processes. There are numerous ways to generate a pore network model, including defining a cubic lattice [10], [11], [12], stochastic methods to produce a topologically equivalent pore networks [13], or extracting

networks from tomography images [14]. A little used method for constructing realistic fibrous structures is to use Delaunay tessellations and Voronoi diagrams [15], [16], [17]. The Delaunay tessellation defines the topology of the pore space i.e. connections between pores, while the Voronoi diagram defines the fiber structure and resulting pore and throat sizes. This approach is well suited to fibrous media since it allows high porosity, high connectivity, and is physically representative.

Anisotropy has been observed in the heat, mass and electrical transport characteristics of GDLs [18], [19], [20]. Carbon paper GDLs tend to have an in-plane alignment of fibers which increases in-plane (IP) transport compared with the through-plane (TP) direction. PNMs representing GDLs have been used to investigate the effects of structural parameters such as anisotropy, heterogeneity and coordination on the effective oxygen diffusivity [11] and the effect of compression on the saturation profile [21], [22], however most studies employ cubic network topologies, so structural parameters can only be adjusted by arbitrarily altering pore and throat sizes in particular directions or regions based on assumptions about the structural changes. While cubic networks are useful for parametric studies they do not fully represent the disordered entangled fibrous structure of common GDLs. The average coordination number of a GDL is higher than that of a regular cubic network and the orientation of throats is not orthogonal. Anisotropy and heterogeneity can easily be varied in a random network when using a Voronoi diagram by scaling the coordinates and adjusting pore density distribution. The average coordination and degree of regularity can also be controlled to an extent with the configuration of the initial pore placement. The effect of compression is also more realistic as changes in the geometry are intrinsically linked to changes in the topology; as pores are moved closer together their throats become smaller and may close off and therefore coordination decreases.

Becker et al. have numerically investigated the effect of compression on multiphase transport using a tomography image of a Toray carbon paper GDL [23]. The image was compressed by shifting voxels designated as fiber and the GeoDict software was used to compute transport properties. Multiphase properties were calculated after filling the image with voxels designated as liquid according to a morphological image opening algorithm [24]. The liquid phase was then assumed to be static and essentially treated as an additional solid phase with no-slip boundary conditions applied to the interfaces. The results show that hydraulic and diffusive transport is reduced with compression with the reduction being more severe for the in-plane direction. The relative transport properties are not explicitly shown in normalized form so it is hard to draw conclusions from the transport curves, although the shape of the curves appears to be unchanged with compression. Becker's study also focuses on uniform compression and so saturation distributions under non-uniform compression introduced by channel geometry are lacking. In this paper, Voronoi-based PNMs are generated and compressed in an effort to study the effects on the transport properties of the GDL. The modelling approach is summarized, networks are validated with comparisons to experimental data and light is shed on the effect of compression on single and multiphase flow. Uniform compression is simulated to systematically study the effects on the relative transport properties of the network. Non-uniform compression is simulated to mimic the impact of flow field compression by adjusting the in-plane porosity profile, and the effect on break-through saturation and limiting current within an operating fuel cell are investigated. It is our aim to present the PNM approach with OpenPNM as a viable method for simulating realistic multiphase behavior over a broad range of compressions within a single modelling framework. In this way models can be built upon incorporating more physical models and investigating a range of materials and geometry scenarios such as the full membrane electrode assembly model recently published by Aghighi et al. [25].

## 2. Model Development

The development of random pore networks using Voronoi diagrams and Delaunay tessellations was undertaken as part of the collaborative open source project OpenPNM ([www.openpnm.org](http://www.openpnm.org)) which has been developed by an international team [26]. The project is written in Python, which is also open source, and makes use of many of the functions for graph theory, computational geometry and image analysis found in Python's SciPy module [27]. This section first describes the process of creating and compressing a disordered network, then describes the percolation algorithm and image analysis approach taken to investigate the effect of compression on multiphase flow. The next part of the section describes how the networks were validated against a morphological approach and experimental drainage data and how the pore scale models that determine the saturation were set. Finally the transport algorithms used to calculate the relative transport characteristics of compressed GDLs are explained.

### 2.1. Network creation

The steps for constructing the networks implemented as part of this study in OpenPNM's *Delaunay* network and *Voronoi* geometry objects are as follows:

- i. Randomly distribute pores in space. For the uncompressed network a domain size of  $750 \times 750 \times 375 \mu\text{m}$  filled with approximately 5000 pores is used. Pores are distributed uniformly but with increased density at the domain edges to counteract the naturally arising higher porosity introduced by the Voronoi method, explained by Gostick [17]. The land-channel results are conducted for networks with a domain size of  $1000 \times 1000 \times 580 \mu\text{m}$  populated with approximately 6000 pores and have a spatially varying porosity in the in-plane x-direction.
- ii. Create throats by connecting nearest neighbor pores according to a Delaunay triangulation and saving the connections in a sparse adjacency matrix.
- iii. Define the fibrous geometry with a Voronoi diagram. This partitions the domain into proximal regions surrounding each pore defined by sets of vertices forming a cage-like structure. This cage is known mathematically as the 'convex hull' of the set of vertices.
- iv. Introduce anisotropy by scaling vertices and pore coordinates. The domain is initially scaled in the z-direction by a factor of 0.82 for uniform compression and 0.5 for the land-channel model to align fibers along the in-plane direction and reduce domain height to 307 and 290  $\mu\text{m}$  respectively. For uniform compression, this scaling was chosen to match porosity and single-phase permeability data for an uncompressed Toray 090 GDL [18].
- v. Create the fibers by populating a binary 3D voxel image with a skeletal frame using a Bresenham line algorithm on the Voronoi vertices. Distance transforms of the voxel image are then performed and re-binarized using a fiber radius of 5  $\mu\text{m}$  as a threshold to expand the skeleton and fill the voxel image with thicker fibers. A section of the final image is shown in Figure (1).
- vi. Populate a similar "hull image" and use this in combination with the fiber image to extract pore and throat sizes by through image analysis. We make use of the convex hull to accurately determine pore volumes, as described in detail by Gostick [17]. Throat areas are also extracted from the images by identifying those lying on the intersections between neighboring pores. An additional distance transform of the fiber image is used to identify those "pore voxels" adjacent to "fiber voxels" in order to calculate pore and throat perimeter lengths.

- vii. Compression is simulated by a manipulation of the fiber image to shift fiber voxels according to their through-plane position as described by Schulz et al. [28], [23], [29]. Compression ratio ( $CR$ ) is defined as percentage reduction in domain height from the 307  $\mu\text{m}$  baseline ( $CR = 1 - l/l_0$ ). Five levels of compression are simulated in 10% step increases from 0% to 50%, the maximal level likely to be experienced within a fuel cell. The land-channel networks remain compressed at 290  $\mu\text{m}$  but contain different pore densities for the different sections.

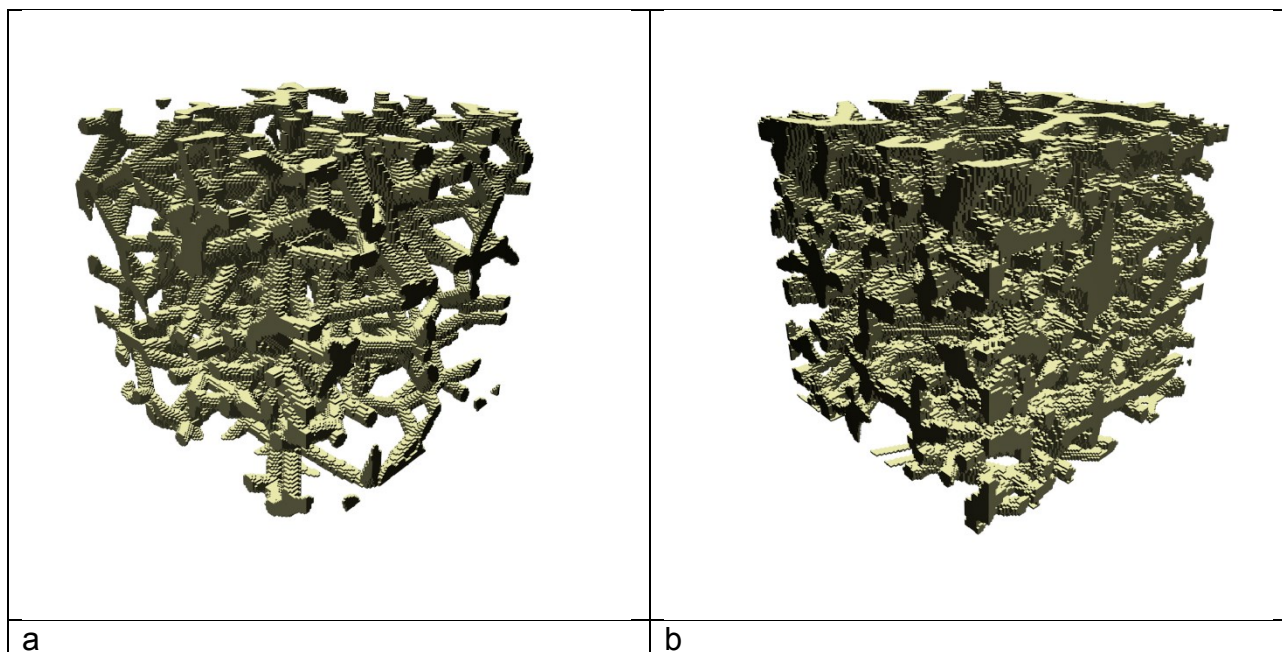


Figure 1: Sections of the fibrous structure generated with a) no compression and b) 50% compression.

OpenPNM provides pore scale models for almost every geometrical parameter. The geometry models implemented in this study are based upon the fiber images generated from the Voronoi diagrams and in most cases are the same as those presented by Gostick [17]. A full description of all the models implemented in this study is included in the Appendix.

## 2.2. Percolation Algorithms

Two percolation algorithms are used in this study: invasion percolation using the generated pore networks and a morphological image analysis performed directly on the fiber image.

### 2.2.1. Invasion Percolation

The percolation algorithm used to determine the placement of liquid water in the network is a modified version of the invasion percolation algorithm (IP) first described by Wilkinson and Willemsen [30] and discussed in the context of fuel cells by Gostick et al. [31]. The algorithm represents drainage of a wetting phase by invasion of a non-wetting phase. This corresponds to the percolation of water in the fuel cell from the catalyst layer at the bottom of the domain to the bipolar plate land or gas channel at the top. This process is typically simulated by starting with an initially dry network and sequentially invading accessible throats belonging to the path of least resistance. Resistance is based on the capillary entry pressure, determined by the Washburn equation, details of which are given in section (2.3).

The algorithm continues until the entire network is filled and trapping of air is not considered as the wetting phase is assumed to form thin films which can always percolate. In the general case IP, when a throat is invaded the pores it connects are assumed to also be filled since pores are larger than throats by definition. In the present case of highly porous anisotropic media with compression, however, some pores were rather flattened and an inscribed sphere was often smaller than some or all of the throats. Consequently, the general IP algorithm was altered such that the entry pressure of both throats and pores were considered when seeking the path of least resistance.

Invasion percolation progresses one element at a time by tracking a list of un-invaded elements connected to the invading cluster, and invading the one with smallest entry pressure. This enables an invasion sequence to be produced which allows the precise determination of saturation at the point of breakthrough. Cluster breakthrough is the point at which an outlet pore at the top of the domain first becomes invaded and represents a percolating pathway, the significance of which is discussed by Gostick et al. [32]. In operating fuel cells the percolating pathways offer less resistance to fluid flow as less pressure is required to inflate a droplet interface growing in the fuel cell gas channels than to invade smaller pores inside the GDL. Therefore, once a pathway is established the breakthrough pattern is often repeated and liquid droplets can be seen forming at the same positions over and over, as modelled by Tranter et al. [1], and observed experimentally by Quesnel et al. [33]. Saturation at breakthrough is therefore a good indication of average medium saturation during fuel cell operation.

Python's *heapq* module provided as part of the standard library is used to manage the list of accessible un-invaded pores and throats efficiently. The heaps are sorted data structures representing a priority queue where the first element (either a pore or throat) always has the smallest value. When a pore is invaded, its newly accessible connecting throats are all added to the queue and sorted by capillary entry pressure automatically. Similarly, when a throat is invaded its connecting pore is added to the queue. The algorithm progresses sequentially removing the most easily accessible pore or throat from the queue, marking the element as invaded with a sequence and cluster number and adding neighbors until the queue is empty and all elements are invaded. The algorithm is a combination of site and bond percolation as pores and throats are treated equally and invaded separately, as opposed to assuming that once a throat is invaded, its connecting pores are also invaded.

For the uniform compression study individual inlet pores are designated for fluid invasion. The inlets are assumed to share the same pressure as if connected to a common external reservoir. We randomly designate 50% of the pores along the bottom face of the network as inlets. Fazeli et al. present a detailed discussion of the different inlet conditions for fuel cell modelling [14] and we consider this to be a fair representation in order to match ex-situ drainage experiments. As Fazeli et al. suggest, percolation through the GDL of operating fuel cells may occur differently with separate liquid clusters growing at different rates. To calculate the breakthrough saturations, in Section (3.3) we apply a cluster inlet condition that groups neighboring inlet pores together. Clusters progress individually but are allowed to merge together and have their own termination condition at the outlet. We randomly choose a number of cluster invasion sites with random grouping radii for our inlet condition. The effect of cluster size is not investigated, but 100 realizations are made for each simulation to ensure statistical representation, and the simulations are repeated for an inlet condition of 10 and 20 clusters.

Once an element is invaded, the volume fraction of each phase is determined heuristically by a late pore filling (LPF) model, described in section (2.3). This decreases the residual air

phase fraction with increasing capillary pressure. A drainage curve can be produced as a post-processing step by summing the volume of the elements with invasion sequence less than a critical step. The critical step corresponds to the first element to be invaded with entry pressure above a critical value. This critical value is incremented from zero to a maximum of 30 MPa in sequence to produce the curves.

In addition to the general compression and transport studies, this work also looks at some fuel-cell specific arrangements. The influence of fuel cell bipolar plate's land to channel ratio is investigated by applying an in-plane porosity gradient to sections of varying size determined by a channel area fraction. The invasion percolation algorithm is run for each network, selecting clusters of pores in the bottom face across the entire domain for liquid water inlets, and all of the pores in the channel section of the top face as outlets. Percolation of each cluster continues until reaching an outlet pore and the total saturation is recorded once all clusters have either reached an outlet pore to form a percolating cluster, or have merged with another cluster.

To investigate the influence of the saturation on the fuel cell performance, we calculate the limiting current by simultaneously performing a percolation and diffusion algorithm, described in Section (2.4). We set the channel boundary condition at 10% oxygen concentration and 0% at the bottom face. The total rate of diffusive flux,  $Q$ , is then calculated by summing the rates of the bottom face pores and converted to a limiting current using Faraday's law:

$$I_{limit} = \frac{4FQ}{A} \quad (1)$$

where  $F$  is Faraday's constant and  $A$  is the area of the bottom face of the network (1mm x 1mm). Our boundary conditions reflect the environment in the cathode of an operating fuel cell running at high current density with humidified gas streams [31].

## 2.2.2. Morphological Image Opening (MIO)

As part of the model validation process a morphological image opening (MIO) algorithm is performed on the binary image of the fibrous structure. The method is outlined by Hilpert and Miller [24] and has been applied to fuel cells several times by Schulz et al. [28], [34] and Gostick [17]. The steps taken are broadly the same as that of Gostick except that routines from SciPy's multi-dimensional image processing tool (*ndimage*) are used as opposed to Matlab:

- i. Using the fiber image produced by OpenPNM's *Voronoi* geometry module as described in section (2.1), we perform a Euclidean distance transform (*dt1*) using the *distance\_transform\_edt* function. This enables the identification of voxels in portions of the pore space at least distance  $r$  from any voxel designated as solid thus creating a skeletal image for the liquid phase.
- ii. Next identify connected clusters of skeletal voxels using the *measurements.label* function on the distance transformed image. Address access limitations by only retaining clusters connected to inlet voxels on the bottom face.
- iii. Perform a second distance transform (*dt2*) on the remaining skeletal clusters using the same radius again to expand the liquid phase.
- iv. Sum the voxels in each phase and correlate this with capillary pressure using the Washburn relation. 0 is solid,  $dt2 \leq r$  is water and  $dt2 > r$  is air.

- v. Decrease  $r$  (i.e. increase capillary pressure) and repeat steps (i) – (iv) until  $r$  is just one voxel length. With a smaller radius the spherical liquid interfaces are able to penetrate smaller features of the voxel image and saturation increases.

MIO naturally accounts for LPF and is used to determine the LPF parameters for the PNM, thus accounting for sub pore-scale features.

### 2.3. Model Validation

To ensure that the PNM is a realistic representation of a GDL steps were taken to validate the modelling approach. To check that pore and throat sizes are being calculated correctly from the fiber image, drainage simulations were performed with each percolation algorithm and are compared below in Figure (2) along with experimental data collected in a previous study by Gostick et al. [2].

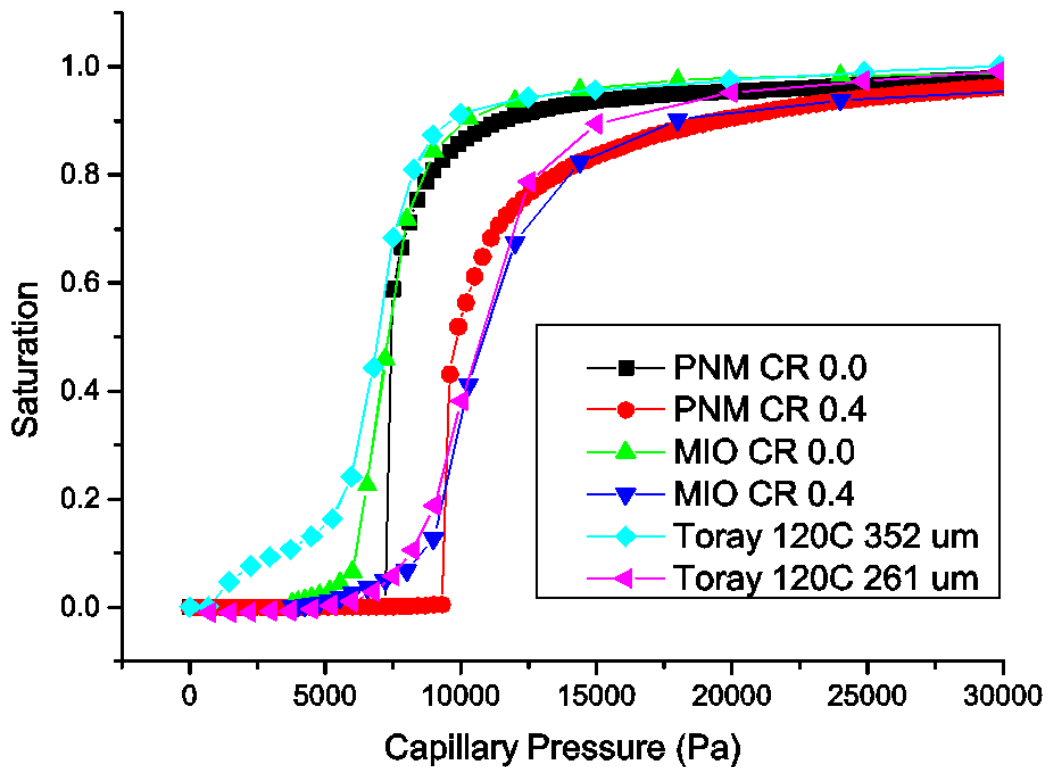


Figure 2: Comparison of drainage curves generated from the PNM and MIO simulations and experiment for Toray 120CGDL under compression.

MIO erodes the pore space with spherical elements of decreasing diameter representing the liquid phase and the capillary pressure is related to the radius ( $r$ ) of the element with the Washburn relation:

$$P_c = -2\sigma \cdot \frac{\cos\theta}{r} \quad (2)$$

A contact angle ( $\theta$ ) of  $120^\circ$  and surface tension ( $\sigma$ ) of  $0.072$  N/m is used. For calculating capillary pressure in the PNM we chose the equivalent diameter because menisci will not

be perfectly spherical but conform to the shape of the constriction. As the PNM algorithm progresses the volume of the residual wetting phase in each pore ( $S_{WP,i}$ ) is determined by a heuristic relation accounting for LPF as follows [17]:

$$S_{WP,i} = S'_{WP} \left( P'_{c,i} / P_c \right)^\eta \quad (3)$$

where  $S'_{WP}$  is a fitting parameter representing the volume fraction of the wetting phase remaining in the pore upon initial invasion at capillary pressure  $P'_{c,i}$  and  $\eta$  is another fitting parameter which determines how quickly the residual wetting phase occupancy decreases inside the pore when increasing capillary pressure. MIO is used to calculate the average fitting parameters for all the pores at each compression ratio by matching Equation (3) to the fraction of occupied voxels inside the pores at each pressure. The fitting parameters are shown in Table (1) below.

<Insert Table 1>

The LPF parameters show that the residual wetting phase upon initial invasion is quite high, and increases with compression. Figuratively, on initial invasion of the pore the invading phase (if non-wetting) may resemble a spherical volume similar in size to an inscribed sphere, although this may bulge out of the pore in reality. As capillary pressure increases, the invading phase will push further into the crevices of the pore space and corners of the pore. As the geometry is compressed, the pore volumes become more skewed, and an inscribed sphere occupies less of the total pore volume fraction, leading to higher wetting phase saturation upon initial pore invasion. The results presented in Figure (2) show close agreement between the two numerical approaches giving confidence to use the generated pore and throat sizes for further pore network modelling.

The uncompressed experimental data shows higher saturation at low capillary pressures compared with the simulations, but this is most likely due to experimental artifacts such as water pooling at the GDL surface due to imperfect contact between the GDL and water injection source. The compressed PNM curve in Figure (2) shows a steeper increase in saturation at around 10,000 Pa than the experimental data, which is most likely due to a narrower distribution in pore and throat sizes used in the model. In reality, fibers may deform and break under compression, leading to the bisection of pores and creation of micro-pores within fibers leading to a larger number of smaller pores. This behavior is beyond the scope of the modelling approach however, and a satisfying level of agreement between datasets is achieved. The MIO results also agree better with experiment when compared with the PNM at low saturations. This is because interfaces are allowed to bulge through the inlet pores without fully invading the pores, and because the medium is thin this effect can contribute to a significant level of saturation.

## 2.4 Transport Algorithms

In addition to percolation algorithms, the single phase and multiphase characteristics of porous media can be studied with PNMs. This is achieved by employing 1D linear transport equations and nodal balances to each set of neighboring pores and then solving the system of equations over the 2D or 3D network. PNMs are therefore similar to resistor networks where hydraulic and diffusive conductivities used to solve Stokes flow and Fickian diffusion are analogous to electrical conductivity used to solve Ohm's Law. The governing equations for mass and species conservation used by OpenPNM as presented by Gostick et al. [9] are

summarized in Table (2). For the conductance values we assume an equivalent spherical and cylindrical shape for pores and throats respectively:

<Insert Table 2>

Both algorithms are implemented in OpenPNM (*StokesFlow*, *FickianDiffusion*) and inherit from a *GenericLinearTransport* object which builds a coefficient matrix based on the supplied conductance models and boundary conditions, then solves it using the standard matrix inversion routines within SciPy. The effective permeability and diffusivity which are intrinsic properties of the networks ( $K_0$  and  $D_{eff}$ ) are then extracted from the predicted flow rates, known domain dimensions, and applied boundary conditions.

Multiphase flow is simulated by effectively solving the equations in each phase separately, where the conductivity of one phase is severely reduced in pores and throats occupied by the other, accomplished by multiplying the single-phase conductance values by a factor of 1E-06. In this way relative transport characteristics can be determined by running transport algorithms at successive stages of the percolation algorithm. A further study of the validity of this conductance assumption could be undertaken, as MIO has revealed that a significant fraction of residual wetting phase exists upon initial invasion which could be conducting. However, this is not the focus of the present study, so it is assumed that corner-filled pockets of air do not effectively conduct.

The conductance values are calculated based on the combined contributions of each half pore, throat, half pore conduit like resistors in series, as is commonly done [9]. Pore centroids and throat centroids are used to calculate the effective pore lengths and the fiber diameter is used as the throat contribution.

### **3. Results and Discussion**

#### **3.1 Size distributions and single phase transport**

The key geometric properties of the networks under compression are shown below and tabulated in the appendix with fitting parameters to a log normal distribution:

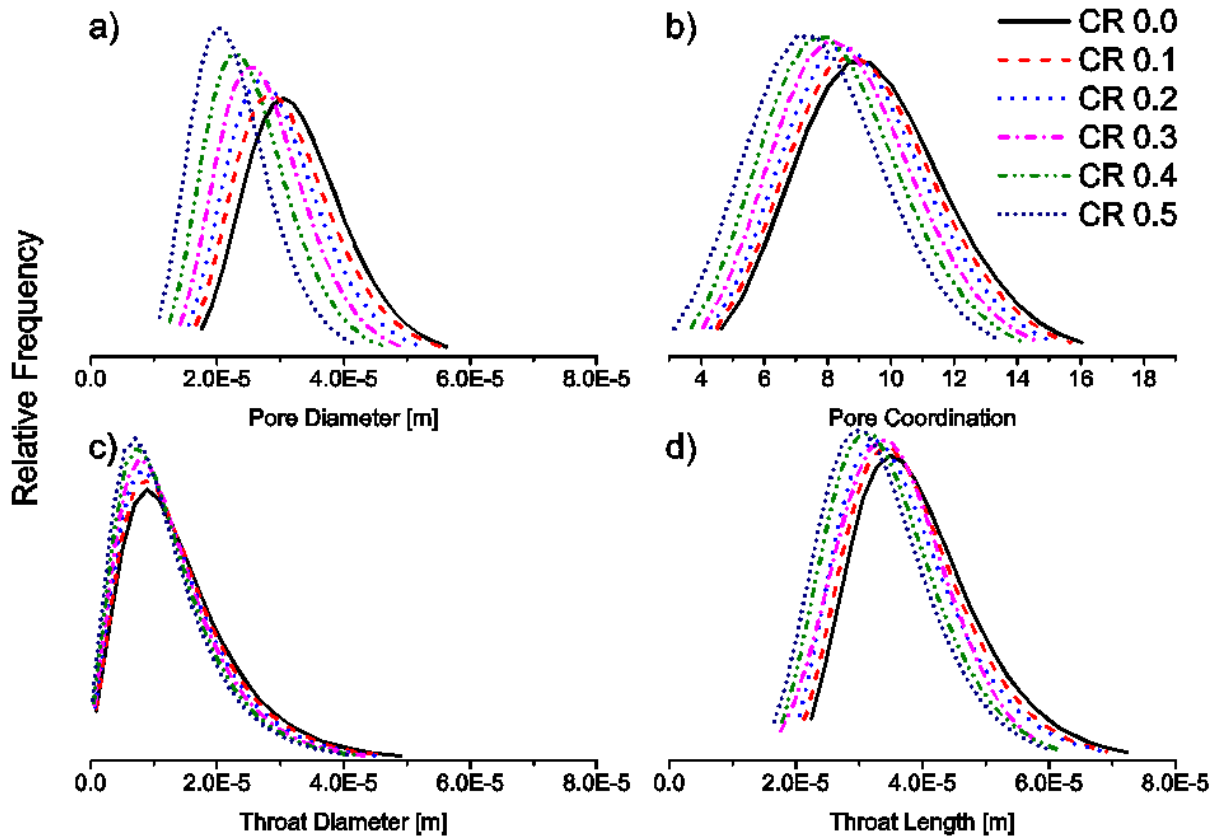


Figure 3: Key network size distributions for all levels of compression.

The general trend is a decrease in all key properties with compression although some changes are more significant than others. Pore diameter is an effective calculation based on the volume of an equivalent sphere. Throat diameter is also an effective calculation based on the area of an equivalent circle. Throat length is the total conduit length used in transport calculations from the centroid of pore  $i$  to the throat center to the centroid of pore  $j$ . Volumes and therefore equivalent diameters of pores reduce the most under compression whereas only a relatively small change in throat lengths is seen. However, as discussed later the change in throat length is different for different directions. Other properties of the network such as contact angle are assumed to remain unchanged with compression.

By also using the throat vector, it is possible to see how the key throat properties that influence the transport change with compression in the different directions. The angle between the throat vector and the through-plane axis is used to group throats and their average properties are normalized by the maximum value in each data set and are plotted with compression below in Figure (4).

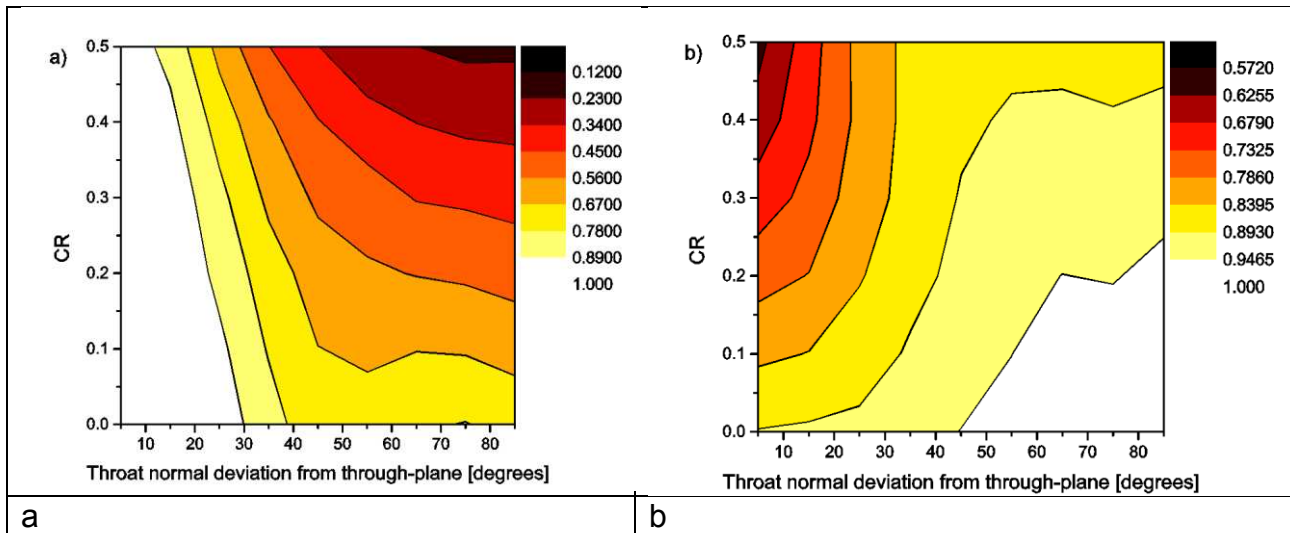


Figure 4: Throat properties averaged by throat normal vector and compression ratio: a) throat area and b) throat length.

Figure (4a) shows that in general the throats aligned with the through-plane direction have the largest area and Figure (4b) shows they have shortest length. The throat area changes significantly for throats aligned with the in-plane direction and not significantly for throats aligned through-plane. In contrast, the throat length does not change significantly with compression in the in-plane direction. On average in-plane throat length reduces by about 20% at most which in-turn reduces in-plane tortuosity slightly. Through-plane throat length scales proportionally with compression ratio as pores are moved closer together and so through-plane tortuosity will remain constant.

Figure (5) shows the effective permeability of the compressed networks for in-plane and through plane directions. Reasonable agreement is found between the simulated data and a Carman-Kozeny relation given as:

$$K = \frac{d_f^2 \varepsilon^3}{16C(1 - \varepsilon)^2} \quad (4)$$

where  $\varepsilon$  is porosity and  $C$  is a fitting parameter. Here a value of 4.07 for  $C$  is used as this was found to be in good agreement for in-plane data collected for Toray090 GDL [18]. We also include data from a study by Becker et al. conducted on samples of Toray 060 GDL [29]. The datasets are similar but the effect of compression on the in-plane permeability seems to be more severe in Becker's study. Toray 060 may have a greater anisotropy than Toray 090 or the differences between the extracted and generated structures or modelling approaches may lead to the difference. For simplicity, we do not include the influence of a shape factor in our hydraulic conductivity which will also change anisotropically with compression and could change the results.

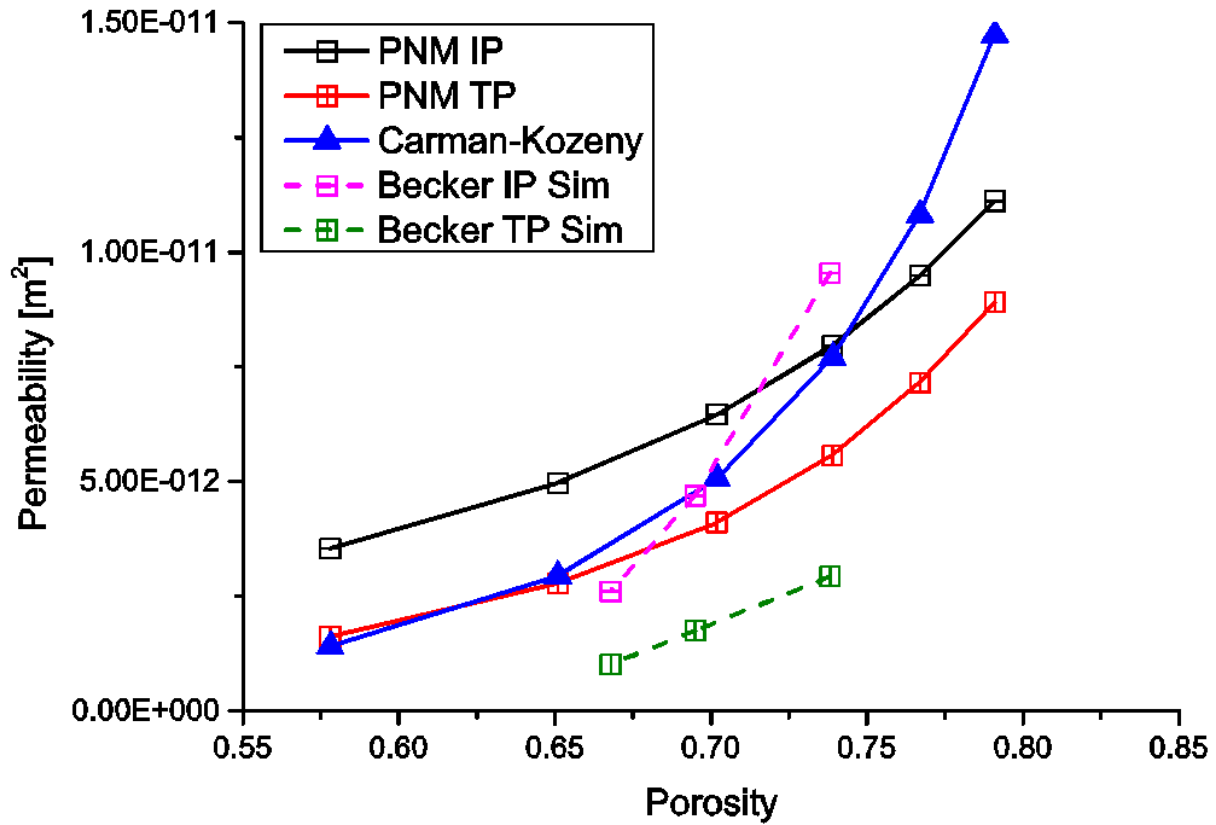


Figure 5: Comparison of single phase effective permeability for uniform compression cases.

Figure (6) shows the effective diffusivity of the compressed networks for in-plane and through-plane directions normalized by the diffusivity of air in open space. The simulated in-plane data is again compared with that of Becker et al. [29] and also with recently obtained experimental in-plane data for Toray090 collected by Rashapov et al. [35]. Encouragingly, good agreement is found between all data sets.

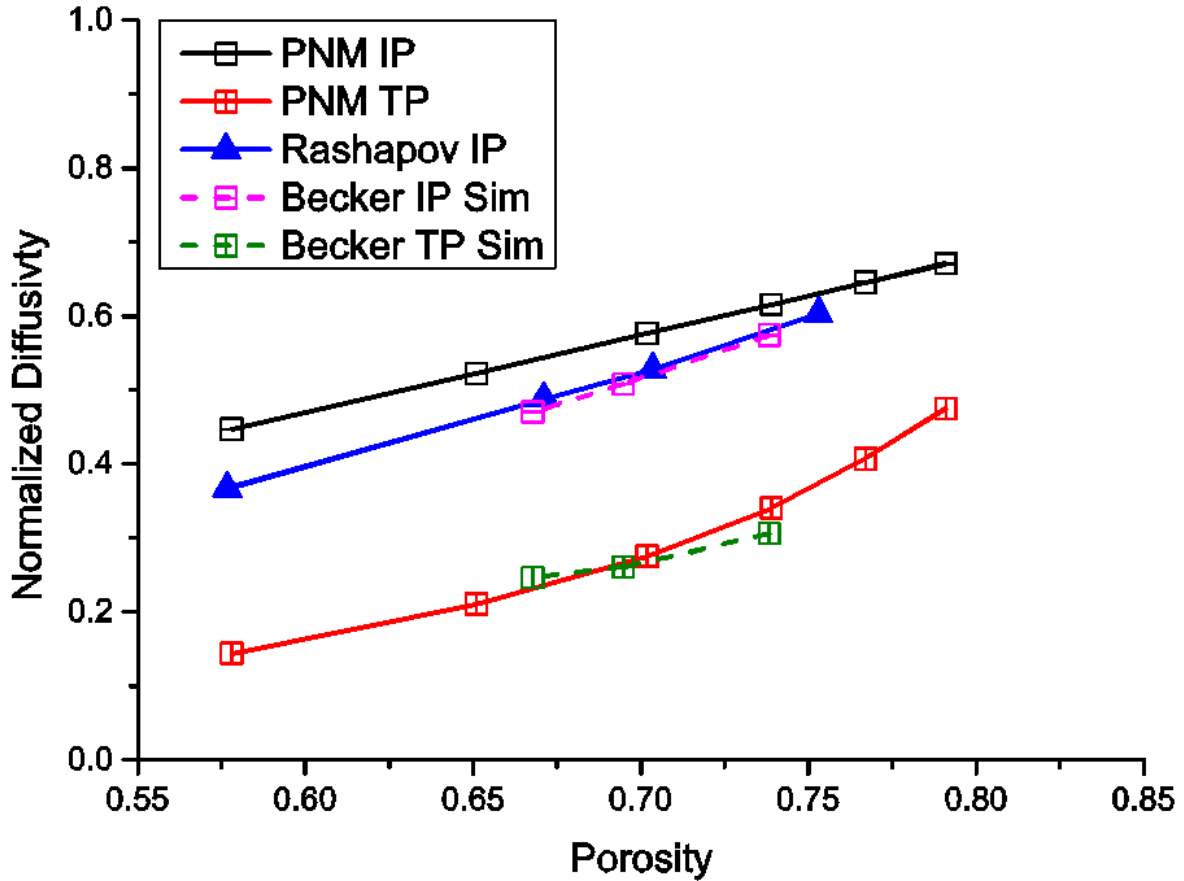


Figure 6: Comparison of single phase effective diffusivity for uniform compression cases.

Both single-phase simulations clearly show the anisotropy in the structures with in-plane values typically double that of through-plane values. As noted by Becker et al. the influence of compression is more greatly felt by the permeability than the diffusivity because permeability depends on the square of the effective pore/throat radius whereas diffusivity is more dependent on the tortuosity which is not found to change significantly.

### 3.2 Multiphase transport under uniform compression

The relative transport properties of each phase are normalized by the transport property with full phase occupancy and are expressed as functions of the liquid phase domain volume fraction i.e. the saturation including late pore filling. The relative transport of mass and species within the air phase is also expressed as a function of a critical saturation or percolation threshold,  $s_c$ , above which no percolating clusters of pores occupied by air are found:

$$\begin{aligned}
 K_a = D_a &= (1 - s)^n \left( \frac{s_c - s}{s_c} \right)^m && (s < s_c) \\
 K_a = D_a &= 0 && (s \geq s_c)
 \end{aligned} \tag{5}$$

The relative permeability of water was found to fit a log normal expression similar to that presented by Hwang & Weber [36] for relative air diffusivity:

$$K_w = \frac{1}{2} \left[ 1 + \operatorname{erf} \left( -\frac{\ln(1-s) + a}{b} \right) \right] \quad (6)$$

100 realizations of each relative property simulation were performed using different randomizations of the inlet boundary pores for percolation.

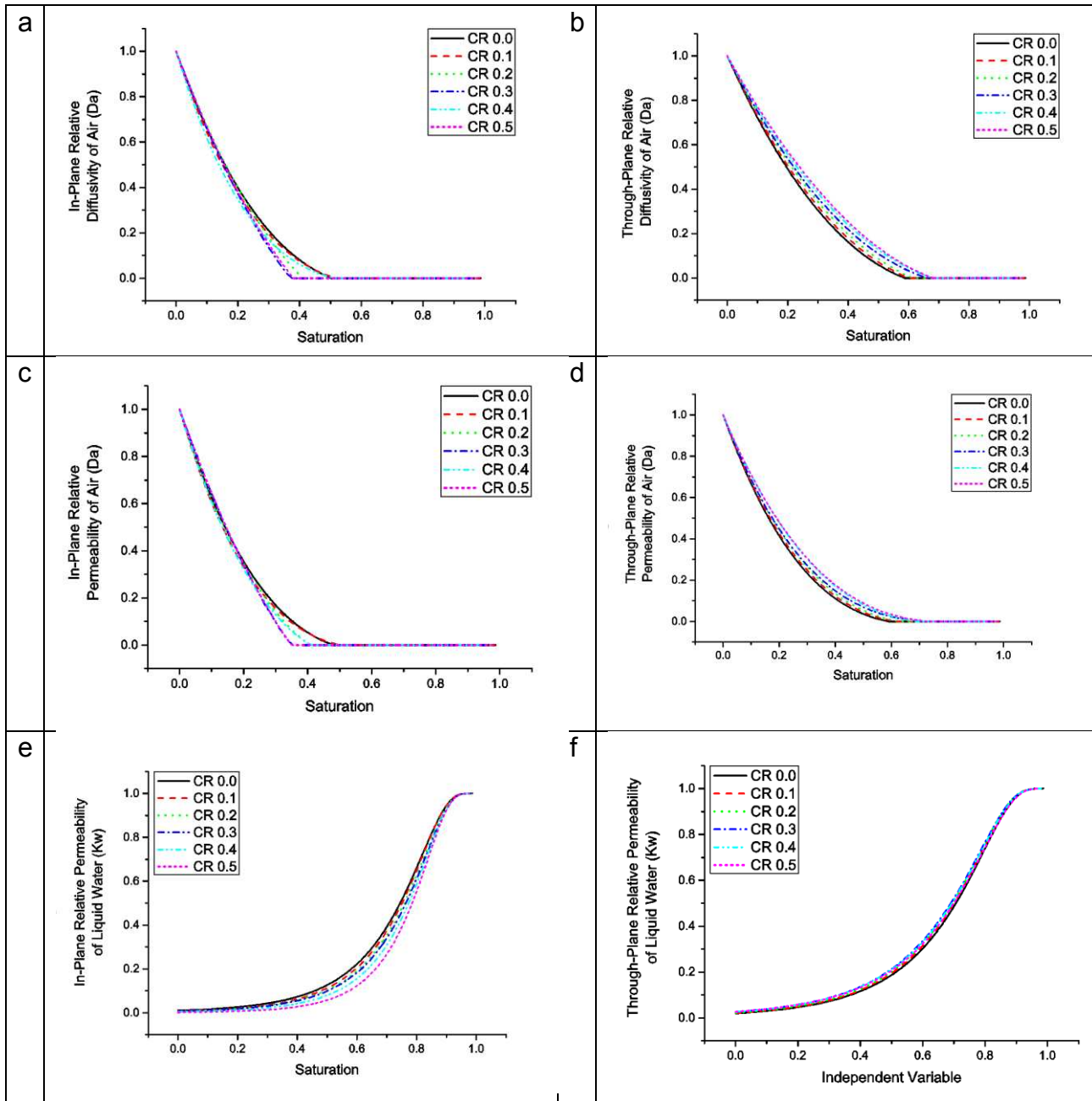


Figure 7: All relative transport relations and their dependence on uniform compression ratio.

Figure (7) shows the dependence of the fitted relative transport expressions on compression of the networks. The pattern for relative air diffusivity is similar to relative air permeability but with slightly lower values. For in-plane relative air transport, the percolation threshold appears to decrease with compression, signifying that transport in the air phase is impeded more significantly at lower saturations under compression. Compression has the opposite effect on through-plane relative air transport which is less impeded at higher saturations compared with in-plane. With increasing compression the difference between in-plane and

through-plane relative air transport widens, as saturation would appear to hamper in-plane transport more significantly. Our results show that an average medium saturation of 0.35 for compressed GDL would result in highly reduced air phase transport in the in-plane direction. Our generated fibrous structures have in-plane fiber alignment but no preferential alignment within the in-plane direction. It is expected that compression would hamper “cross-fiber” transport much more severely than “along-fiber” transport. It would be possible to construct fully 3-dimensionally anisotropic networks using the Voronoi approach through scaling of the vertices but this is left for future work.

For liquid permeability we see a decrease in the in-plane relative transport and relatively little change in the through-plane transport. Given the initial anisotropy in the networks, which show in-plane conductance typically twice that of through-plane, the results suggest that as networks start becoming saturated this anisotropy is assuaged and the effect increases with compression. The reason for this re-balancing of through-plane and in-plane transport can be explained by the relative change in throat area for the different directions shown in Figure (4). Throats that are orientated more towards in-plane close off quicker than those orientated through-plane and therefore capillary pressure increases and the path of least resistance points more towards the through-plane direction.

### **3.3 Multiphase transport with in-plane porosity gradient**

The results shown in the previous two sections were produced using uniformly compressed networks. The GDL is not generally compressed uniformly when assembling the fuel cell as current collector flow fields are grooved and present a series of channels and lands as reviewed by Hamilton and Pollet [37]. The lands make contact with the GDL and reduce the porosity, creating in-plane porosity gradients. Networks are created with lowered pore density in a central region of the domain with varying width, representing the GDL beneath a channel in the bipolar plate of a fuel cell. The land width to channel width ratio is set at 3:1, 2:1, 1:1, 1:2 & 1:3 and is expressed in our figures as a channel area fraction. Pores in the channel region are further apart and consequently have larger volumes and so the region has higher porosity.

The influence of the channel area fraction on the breakthrough saturation is shown in Figure (8). There is no discernible pattern and little variation with channel area fraction. There also appears to be little difference in the total saturation of the medium when varying the number of inlet clusters. No attempt to correlate the inlet cluster positions with the position of the lands is made, and only percolation from the bottom face is considered.

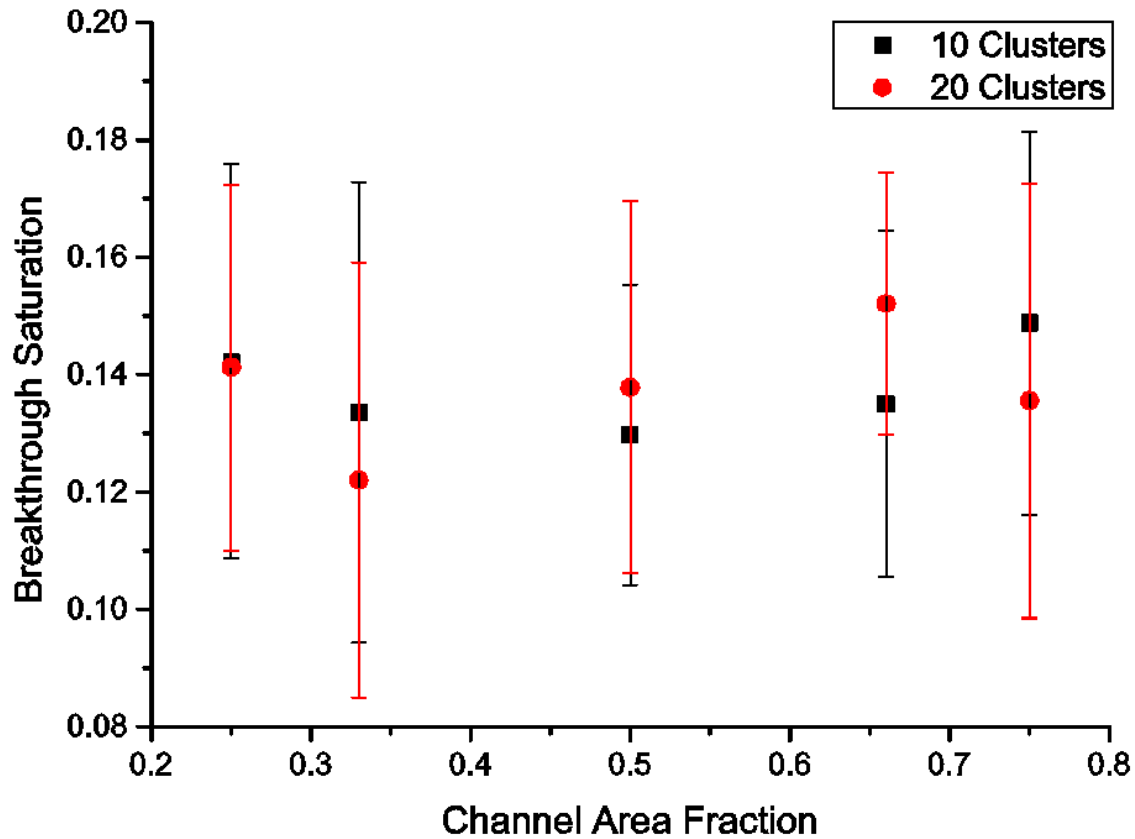


Figure 8: Break-through saturation for non-uniform compression with land- channel boundary conditions and different numbers of clusters.

The in-plane saturation profiles produced by our simulations agree well with x-ray computed tomography data collected by Zenyuk et al. [38], conducted ex-situ under isothermal conditions. The bulk of the liquid tends to collect in the higher porosity section of GDL beneath the channel. However, under non-isothermal conditions such as those typically encountered within a fuel cell, the liquid may condense under the cooler rib sections and evaporate where convection is strongest under the channels [39], [40]. Two recent pore network studies that investigated phase change phenomena support this hypothesis, but did not account for porosity variation or local pore structure changes due to compression [41], [42]. Further work is required to assess the relative importance of the competing transport effects on the liquid percolation under different operating fuel cell conditions.

Figure (9) shows the influence of both the channel area fraction and number of inlet clusters on the limiting current. The dry results with no water in the network show that as the channel area fraction is increased, the limiting current also increases. This result is intuitive as the area open to flow is increasing and so diffusive flux is greater. Introducing water reduces the diffusive conductivity of the network, as shown in the previous section, but the influence of the saturation distribution also becomes clearer.

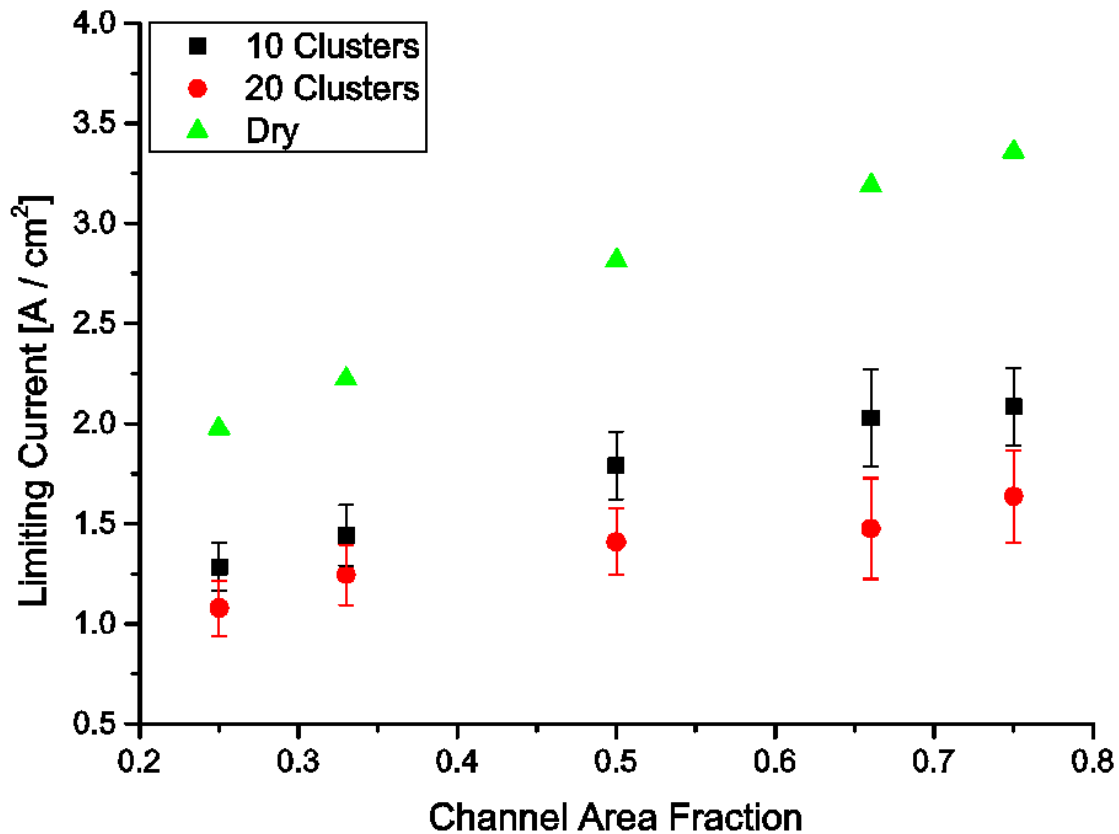


Figure 9: Limiting current for non-uniform compression with land-channel boundary conditions and different numbers of clusters.

Although the total domain saturation at break-through is relatively similar for the 10 and 20 cluster inlet conditions, the distribution of saturation is skewed more towards the inlets at the bottom face for the 20 cluster condition, as shown in Figure (10). This in turn creates more of a bottleneck for diffusive transport and reduces the rate at which oxygen can flow to the bottom face. Hence the limiting current is reduced compared with the 10 cluster simulations. This situation demonstrates one of the effects of introducing an MPL to the bottom face of the GDL, which acts to reduce the number of percolating clusters, and therefore reduces the bottleneck effect. A recent study by García-Salaberri et al. using the Lattice Boltzmann technique also supports these findings [43]. It would seem that peak saturation is a stronger indicator of fuel cell performance than average saturation, and modelling techniques that can accurately re-produce saturation profiles should be used to predict fuel cell performance. Although our inlet condition is not dependent on the level of compression or position within the domain, one might expect the entry points into the GDL to depend on cracks in the MPL which are more likely to occur beneath the land. Compression is also important for the contact between layers which, if poor, will result in liquid pooling at interfaces leading to severe bottle-necks for air transport as discussed by Simon et al. [44].

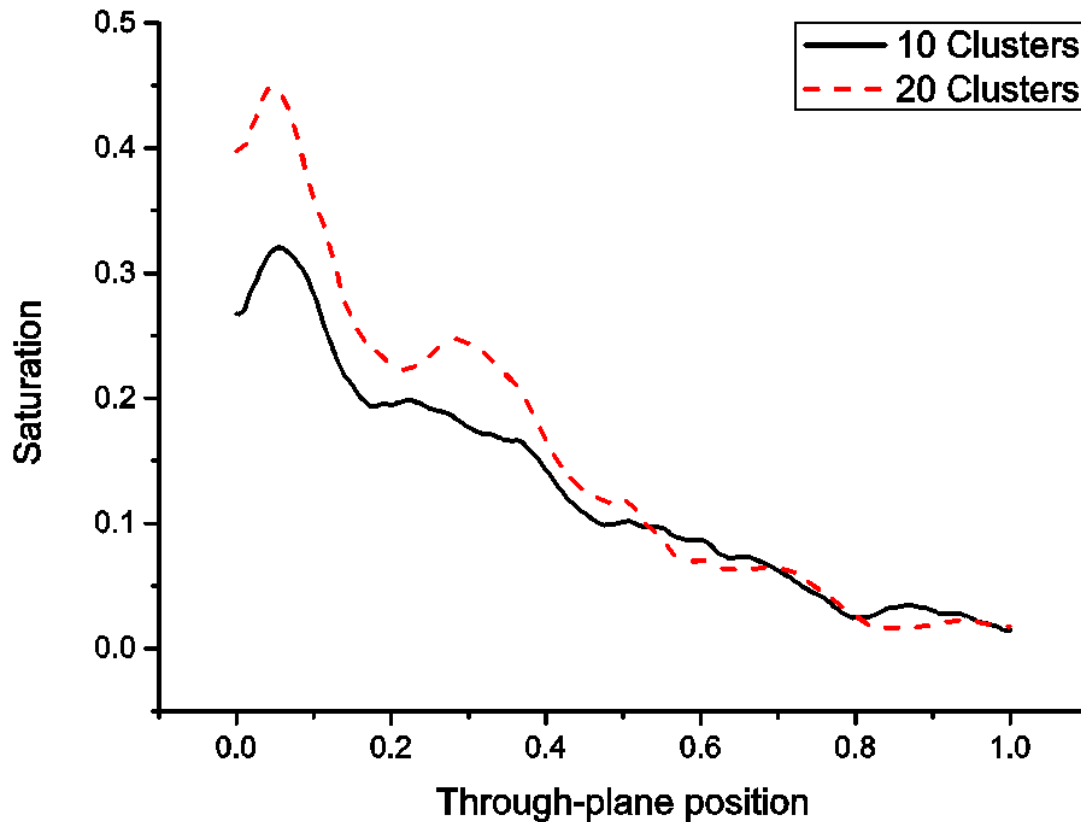


Figure 10: Through-plane saturation profile for the different cluster conditions with a channel area fraction of 0.5.

#### 4. Conclusion

A series of PNMs subject to compression are presented, with good agreement to experimental drainage and single phase transport data. Effective and relative transport simulations are performed, and the effect of compression is shown to reduce effective transport but increase some relative transport, depending on the direction and phase. It is found that compression has a more adverse effect on the in-plane transport than through-plane and this can be explained by considering the different structural changes to constrictions between fibers.

In-plane porosity variation under a land-channel-land scenario is shown to affect the liquid percolation pathway with a strong correlation between saturation and porosity. This in turn affects the limiting current achievable with a fuel cell which increases proportionally with the channel area fraction, and decreases with the number of inlet clusters. PNMs are demonstrated as powerful tools capable of characterizing porous materials with great efficiency and accuracy.

It is recommended that further investigation into the land-channel influence on transport in the GDL is conducted combining the topological considerations presented here and the phase change considerations presented elsewhere. It is hoped that performing simulations with OpenPNM, an open source framework developed as part of this work, will aid future investigations.

## Acknowledgements:

The authors would like to thank the EPSRC for the grant funding to carry out this work and AFCC for contributing to the development of OpenPNM.

## Nomenclature:

A	$m^2$	Network cross-sectional area
c	$\text{mol m}^{-1}$	Concentration
D	$m^2 \text{ s}^{-1}$	Diffusivity
$d_f$	m	Fiber diameter
F	$C \text{ mol}^{-1}$	Faraday's Constant
$g_d$	$m^3 \text{ s}^{-1}$	Diffusive conductivity
$g_h$	$m^3 \text{ Pa}^{-1} \text{ s}^{-1}$	Hydraulic conductivity
K	$m^2$	Permeability
l	m	Conduit Length
L	m	Network Length
$n_a$	$\text{mol s}^{-1}$	Diffusion rate of species a through conduit
$N_a$	$\text{mol s}^{-1}$	Diffusion rate of species a through network
P	Pa	Pressure
q	$m^3 \text{ s}^{-1}$	Flow through conduit
Q	$m^3 \text{ s}^{-1}$	Flow through network
r	m	Conduit radius
s	-	Saturation
x	-	Mole fraction

## Greek:

$\epsilon$	-	Porosity
$\sigma$	$\text{N m}^{-1}$	Surface tension
$\theta$	degrees	Contact angle
$\eta$	-	Late pore filling exponent

## Subscripts:

0	Uncompressed
C	Capillary
d	Diffusive
h	Hydraulic
ij	Between pore i and j
in	Inlet
out	Outlet
c	critical
f	fiber
WP	Wetting Phase

## Bibliography

- [1] T. G. Tranter, A. D. Burns, D. B. Ingham and M. Pourkashanian, "The effects of compression on single and multiphase flow in a model polymer electrolyte membrane fuel cell gas diffusion layer," *International Journal of Hydrogen Energy*, vol. 40, pp. 652-664, 2015.
- [2] J. T. Gostick, M. A. Ioannidis, M. W. Fowler and M. D. Pritzker, "Wettability and capillary behavior of fibrous gas diffusion media for polymer electrolyte membrane fuel cells," *Journal of Power Sources*, vol. 194, no. 1, pp. 433-444, 2009.
- [3] A. Bazylak, D. Sinton, Z. S. Liu and N. Djilali, "Effect of compression on liquid water transport and microstructure of PEMFC gas diffusion layers," *Journal of Power Sources*, vol. 163, no. 2, pp. 784-792, 2007.
- [4] M. Mortazavi and K. Tajiri, "Liquid water breakthrough pressure through gas diffusion layer of proton exchange membrane fuel cell," *International Journal of Hydrogen Energy*, vol. 39, no. 17, pp. 9409-9419, 2014.
- [5] B. Ramos-Alvarado, J. D. Sole, A. Hernandez-Guerrero and M. W. Ellis, "Experimental characterization of the water transport properties of PEM fuel cells diffusion media," *Journal of Power Sources*, vol. 218, pp. 221-232, 2012.
- [6] H. Markötter, K. Dittmann, J. Haußmann, R. Alink, D. Gerteisen, H. Riesemeier, J. Scholta, J. Banhart and I. Manke, "Influence of local carbon fibre orientation on the water transport in the gas diffusion layer of polymer electrolyte membrane fuel cells," *Electrochemistry Communications*, vol. 51, pp. 133-136, 2015.
- [7] P. K. Sinha and C.-Y. Wang, "Pore-network modeling of liquid water transport in gas diffusion layer of a polymer electrolyte fuel cell," *Electrochimica Acta*, vol. 52, no. 28, pp. 7936-7945, 2007.
- [8] A. Putz, J. Hinebaugh, M. Aghighi, H. Day, A. Bazylak and J. T. Gostick, "Introducing OpenPNM: An open source pore network modeling software package," *ECS Transactions*, vol. 58, no. 1, pp. 79-86, 2013.
- [9] J. T. Gostick, M. A. Ioannidis, M. W. Fowler and M. D. Pritzker, "Pore network modeling of fibrous gas diffusion layers for polymer electrolyte membrane fuel cells," *Journal of Power Sources*, vol. 173, no. 1, pp. 277-290, 2007.
- [10] M. Rebai and M. Prat, "Scale effect and two-phase flow in a thin hydrophobic porous layer. Application to water transport in gas diffusion layers of proton exchange membrane fuel cells," *Journal of Power Sources*, vol. 192, no. 2, pp. 534-543, 2009.
- [11] R. Wu, X. Zhu, Q. Liao, H. Wang, Y. d. Ding, J. Li and D. D. Ye, "Determination of oxygen effective diffusivity in porous gas diffusion layer using a three-dimensional pore network model," *Electrochimica Acta*, vol. 55, no. 24, pp. 7394-7403, 2010.
- [12] A. Bazylak, V. Berejnov, B. Markicevic, D. Sinton and N. Djilali, "Numerical and microfluidic pore networks: Towards designs for directed water transport in GDLs," *Electrochimica Acta*, vol. 53, no. 26, pp. 7630-7637, 2008.
- [13] G. Luo, Y. Ji, C. Y. Wang and P. K. Sinha, "Modeling liquid water transport in gas diffusion layers by topologically equivalent pore network," *Electrochimica Acta*, vol. 55, no. 19, pp. 5332-5341, 2010.
- [14] M. Fazeli, J. Hinebaugh and A. Bazylak, "Investigating Inlet Condition Effects on PEMFC GDL Liquid Water Transport through Pore Network Modeling," *ECS Transactions*, vol. 64, no. 3, pp. 593-602, 2014.
- [15] K. E. Thompson, "Pore-scale modeling of fluid transport in disordered fibrous materials," *AIChE Journal*, vol. 48, no. 7, pp. 1369-1389, 2002.
- [16] J. Hinebaugh, Z. Fishman and A. Bazylak, "Unstructured Pore Network Modeling with Heterogeneous PEMFC GDL Porosity Distributions," *Journal of The Electrochemical Society*, vol. 157, no. 11, pp. B1651-B1657, 2010.

- [17] J. T. Gostick, "Random Pore Network Modeling of Fibrous PEMFC Gas Diffusion Media Using Voronoi and Delaunay Tessellations," *Journal of the Electrochemical Society*, vol. 160, no. 8, pp. F731-F743, 2013.
- [18] J. T. Gostick, M. W. Fowler, M. D. Pritzker, M. A. Ioannidis and L. M. Behra, "In-plane and through-plane gas permeability of carbon fiber electrode backing layers," *Journal of Power Sources*, vol. 162, no. 1, pp. 228-238, 2006.
- [19] M. Ismail, K. Hughes, D. Ingham, L. Ma and M. Pourkashanian, "Effects of anisotropic permeability and electrical conductivity of gas diffusion layers on the performance of proton exchange membrane fuel cells," *Applied Energy*, vol. 95, pp. 50-63, 2012.
- [20] N. Alhazmi, D. Ingham, M. Ismail, K. Hughes, L. Ma and M. Pourkashanian, "Effect of the anisotropic thermal conductivity of GDL on the performance of PEM fuel cells," *International Journal of Hydrogen Energy*, vol. 38, no. 1, pp. 603-611, 2013.
- [21] K.-J. Lee, J. H. Nam and C.-J. Kim, "Pore-network analysis of two-phase water transport in gas diffusion layers of polymer electrolyte membrane fuel cells," *Electrochimica Acta*, vol. 54, no. 4, pp. 1166-1176, 2009.
- [22] M. Rebai and M. Prat, "Scale effect and two-phase flow in a thin hydrophobic porous layer. Application to water transport in gas diffusion layers of proton exchange membrane fuel cells," *Journal of Power Sources*, vol. 192, no. 2, pp. 534-543, 2009.
- [23] J. Becker, V. Schulz and A. Weigmann, "Numerical Determination of Two-Phase Material Parameters of a Gas Diffusion Layer Using Tomography Images," *Journal of fuel cell science and technology*, vol. 5, no. 2, p. 021006, 2008.
- [24] M. Hilpert and C. T. Miller, "Pore-morphology-based simulation of drainage in totally wetting porous media," *Advances in Water Resources*, vol. 24, no. 3-4, pp. 243-255, 2001.
- [25] M. Aghighi, M. A. Hoeh, W. Lehnert, G. Merle and J. Gostick, "Simulation of a Full Fuel Cell Membrane Electrode Assembly Using Pore Network Modeling," *Journal of The Electrochemical Society*, vol. 163, no. 5, pp. F384-F392, 2016.
- [26] J. T. Gostick, M. Aghighi, J. Hinebaugh, T. G. Tranter, M. Hoh, H. Day, A. Bazylak, A. D. Burns, W. Lehnert and A. Putz, "OpenPNM: A Pore Network Modeling Package," *Computing in Science & Engineering*, vol. 18, no. 4, pp. 60-74, 2016.
- [27] E. Jones, T. Oliphant and P. Peterson, "SciPy: Open source scientific tools for Python," 2001. [Online]. Available: <http://www.scipy.org/>.
- [28] V. P. Schulz, J. Becker, A. Wiegmann, P. P. Mukherjee and C.-Y. Wang, "Modeling of Two-Phase Behavior in the Gas Diffusion Medium of PEFCs via Full Morphology Approach," *Journal of The Electrochemical Society*, vol. 154, no. 4, pp. B419-B426, 2007.
- [29] J. Becker, R. Flückiger, M. Reum, F. N. Büchi, F. Marone and M. Stampanoni, "Determination of Material Properties of Gas Diffusion Layers: Experiments and Simulations Using Phase Contrast Tomographic Microscopy," *Journal of The Electrochemical Society*, vol. 156, no. 10, pp. B1175-B1181, 2009.
- [30] D. Wilkinson and J. F. Willemsen, "Invasion percolation: a new form of percolation theory," *Journal of Physics A: Mathematical and General*, vol. 16, no. 14, pp. 3365-3376, 1983.
- [31] J. T. Gostick, M. A. Ioannidis, M. D. Pritzker and M. W. Fowler, "Impact of Liquid Water on Reactant Mass Transfer in PEM Fuel Cell Electrodes," *Journal of the Electrochemical Society*, vol. 157, no. 4, pp. B563-B571, 2010.
- [32] J. T. Gostick, M. A. Ioannidis, M. W. Fowler and M. D. Pritzker, "Characterization of the Capillary Properties of Gas Diffusion Media," in *Modern Aspects of Electrochemistry 49*, Berlin, Springer, 2010, pp. 225-254.
- [33] C. Quesnel, R. Cao, J. Lehr, A.-M. Kietzig, A. Z. Weber and J. T. Gostick, "Dynamic Percolation and Droplet Growth Behavior in Porous Electrodes of Polymer Electrolyte Fuel Cells," *The Journal of Physical Chemistry C*, vol. 119, no. 40, pp. 22934-22944, 2015.

- [34] V. P. Schulz, E. A. Wargo and E. C. Kumbur, "Pore-Morphology-Based Simulation of Drainage in Porous Media Featuring a Locally Variable Contact Angle," *Transport in Porous Media*, vol. 107, no. 1, pp. 13-25, 2015.
- [35] R. Rashapov and J. T. Gostick, "In-plane effective diffusivity in PEMFC gas diffusion layers," *Transport in Porous Media*, pp. 1-23, 2016.
- [36] G. S. Hwang and A. Z. Weber, "Effective-Diffusivity Measurement of Partially-Saturated Fuel-Cell Gas-Diffusion Layers," *Journal of the Electrochemical Society*, vol. 159, no. 11, pp. F683-F692, 2012.
- [37] P. Hamilton and B. Pollet, "Polymer Electrolyte Membrane Fuel Cell (PEMFC) Flow Field Plate: Design, Materials and Characterisation," *Fuel Cells*, vol. 10, no. 4, pp. 489-589, 2010.
- [38] I. V. Zenyuk, D. Y. Parkinson, G. Hwang and A. Weber, "Probing water distribution in compressed fuel-cell gas-diffusion layers using X-ray computed tomography," *Electrochemistry Communications*, vol. 53, pp. 22-28, 2015.
- [39] Y. Tabuchi, T. Shiomi, O. Aoki, N. Kubo and K. Shinohara, "Effects of heat and water transport on the performance of polymer electrolyte membrane fuel cell under high current density operation," *Electrochimica Acta*, vol. 56, pp. 352-360, 2010.
- [40] T. Rosén, J. Eller, J. Kang, N. I. Prasianakis, J. Mantzaras and F. N. Büchi, "Saturation Dependent Effective Transport Properties of PEFC Gas Diffusion Layers," *Journal of the Electrochemical Society*, vol. 159, no. 9, pp. F536-F544, 2012.
- [41] B. Straubhaar, J. Pauchet and M. Prat, "Water transport in gas diffusion layer of a polymer electrolyte fuel cell in the presence of a temperature gradient. Phase change effect," *International Journal of Hydrogen Energy*, p. (In Press), 2015.
- [42] C. Qin, "Water Transport in the Gas Diffusion Layer of a Polymer Electrolyte Fuel Cell: Dynamic Pore-Network Modeling," *Journal of the Electrochemical Society*, vol. 162, no. 9, pp. F1036-F1046, 2015.
- [43] P. A. García-Salaberri, G. Hwang, M. Vera, A. Z. Weber and J. T. Gostick, "Effective diffusivity in partially-saturated carbon-fiber gas diffusion layers: Effect of through-plane saturation distribution," *International Journal of Heat and Mass Transfer*, vol. 86, pp. 319-333, 2015.
- [44] C. Simon, F. Hasché, D. Müller and H. A. Gasteiger, "Influence of the Gas Diffusion Layer Compression on the Oxygen Mass Transport in PEM Fuel Cells," *ECS Transactions*, vol. 69, no. 17, pp. 1293-1302, 2015.
- [45] Z. Fishman, J. Hinebaugh and A. Bazylak, "Microscale Tomography Investigations of Heterogeneous Porosity Distributions of PEMFC GDLs," *Journal of The Electrochemical Society*, vol. 157, no. 11, pp. B1643-B1650, 2010.
- [46] D. Silin and T. Patzek, "Pore space morphology analysis using maximal inscribed spheres," *Physica A*, vol. 371, p. 336-360, 2006.
- [47] H. J. Vogel, J. Tölke, V. P. Schulz, M. Krafczyk and K. Roth, "Comparison of a Lattice-Boltzmann Model, a Full-Morphology Model, and a Pore Network Model for Determining Capillary Pressure-Saturation Relationships," *Vadose Zone Journal*, vol. 4, no. 2, pp. 380-388, 2005.
- [48] N. Mortensen, F. Okkels and H. Bruus, "Reexamination of Hagen-Poiseuille flow: Shape dependence of the hydraulic resistance in microchannels," *Physical Review E*, vol. 71, no. 5, p. 057301, 2005.
- [49] R. Wu, Q. Liao, X. Zhu and H. Wang, "Impacts of the mixed wettability on liquid water and reactant gas transport through the gas diffusion layer of proton exchange membrane fuel cells," *International Journal of Heat and Mass Transfer*, vol. 55, no. 9, pp. 2581-2589, 2012.

[50] J. T. Gostick, M. A. Ioannidis, M. D. Pritzker and M. W. Fowler, "Impact of Liquid Water on Reactant Mass Transfer in PEM Fuel Cell Electrodes," *Journal of The Electrochemical Society*, vol. 157, no. 4, pp. B563-B571, 2010.

Tables:

Compression Ratio	S'WP	$\eta$
0.0	0.312	4.00
0.1	0.317	3.30
0.2	0.321	2.87
0.3	0.333	2.56
0.4	0.370	2.35
0.5	0.421	2.08

Table 1: The late pore filling parameters for different compression ratios determined from morphological image analysis

Pore Level Conservation	Conductance	Network Level Conservation
$\sum_{j=1}^n q_{ij} = \sum_{j=1}^n g_{h,ij} (P_j - P_i)$	$g_h = \frac{\pi r^4}{4l\mu}$	$Q = \frac{K_0 A}{\mu L} (P_{in} - P_{out})$
$\sum_{j=1}^n n_{a,ij} = \sum_{j=1}^n g_{d,ij} (\ln x_{a,j} - \ln x_{a,i})$	$g_d = \frac{cD_{ab}r^2}{4l}$	$N_a = \frac{cD_{eff}A}{L} (\ln x_{a,in} - \ln x_{a,out})$

Table 2: Governing Conservation Equations

## Appendix

CR	Shape	Location	Scale
0.00	2.17E-01	-4.67E-06	3.68E-05
0.10	2.69E-01	8.27E-07	2.96E-05
0.20	2.55E-01	-8.11E-07	2.95E-05
0.30	2.34E-01	-3.45E-06	3.03E-05
0.40	2.49E-01	-2.88E-06	2.74E-05
0.50	2.60E-01	-2.41E-06	2.43E-05

Table A1: Pore diameter fitted parameters under compression using the *lognorm* distribution from SciPy's statistics routines.

CR	Shape	Location	Scale
0.00	1.52E-01	-6.49E+00	1.58E+01
0.10	1.56E-01	-6.02E+00	1.51E+01
0.20	1.51E-01	-6.38E+00	1.52E+01
0.30	1.48E-01	-6.74E+00	1.52E+01
0.40	1.42E-01	-7.51E+00	1.56E+01
0.50	1.21E-01	-1.05E+01	1.81E+01

Table A2: Pore coordination fitted parameters under compression using the *lognorm* distribution from SciPy's statistics routines.

CR	Shape	Location	Scale
0.00	4.89E-01	-4.52E-06	1.71E-05
0.10	4.89E-01	-4.42E-06	1.65E-05
0.20	4.85E-01	-4.46E-06	1.60E-05
0.30	4.84E-01	-4.40E-06	1.55E-05
0.40	4.91E-01	-4.27E-06	1.48E-05
0.50	5.02E-01	-4.12E-06	1.41E-05

Table A3: Throat diameter fitted parameters under compression using the *lognorm* distribution from SciPy's statistics routines.

CR	Shape	Location	Scale
0.00	3.32E-01	8.77E-06	2.93E-05
0.10	3.12E-01	6.69E-06	3.02E-05
0.20	3.52E-01	8.83E-06	2.66E-05
0.30	1.45E-01	-2.59E-05	6.09E-05
0.40	2.61E-01	-7.59E-07	3.40E-05
0.50	2.56E-01	-2.33E-06	3.43E-05

Table A4: Throat length fitted parameters under compression using the *lognorm* distribution from SciPy's statistics routines.

Property	Description
Pore Volume	The convex hull in 3d of the Voronoi vertices surrounding each pore, the pore hull

Pore Centroid	The position of the local maximum of a distance transform on the whole fiber image for the voxels contained in the pore hull
Pore Diameter	The equivalent diameter of a sphere with equal pore volume
Pore In(scribed)-diameter	Twice the maximum of the distance transform used to calculate the pore centroid
Pore Area	Cross sectional area based on an equivalent circle using the pore diameter
Throat Area	The intersection between neighboring pore hulls in the voxel image
Throat Vector	Vector normal to the throat plane defined by the Voronoi vertices
Throat Perimeter	Length of the splines between the vertices after image erosion by the fiber radius
Throat Centroid	As with Pore Centroid but for voxels on the intersection between neighboring pore hulls
Throat Diameter	The equivalent diameter of a circle with equal throat area
Throat In(scribed)-diameter	Twice the maximum of the distance transform used to calculate the throat centroid
Throat Length	The center to center length from the connecting pore centroids passing the throat centroid
Throat Volume	An extrusion volume of the throat area of length equal to the fiber radius

Table A5: Pore and throat geometry models implemented in OpenPNM as part of the Voronoi geometry.